Propagation in Extended Highly Anisotropic Media

Charles Rino[1], **Charles Carrano**[1], **Keith Groves**[1]

[1]Institute for Scientific Research, Boston College, Boston, MA, USA.

Key Points:

- Configuration-space realizations are summations of field-aligned *striations* with parameter distributions that support two-component inverse power-law spectral characterization.
- Configuration-space realizations are well suited for studying propagation in extended highly anisotropic ionospheric media.
- This paper revisits the geometric dependence of propagation in highly anisotropic media with emphasis on structure models and interpreting diagnostic measurements.

Corresponding author: Charles Rino, `crino@bc.edu`

Abstract

Configuration-space realizations, which are summations of elemental magnetic-field-aligned striations, were introduced to explore propagation in extended anisotropic media. Global Navigation Satellite System (GNSS) measurements are of particular interest because the propagation paths from GNSS satellites to low-earth-orbiting satellites transition extended regions of ionospheric structure. Configuration-space realizations can have any orientation within the simulation volume. Rotating the structure relative to the principal propagation direction varies the propagation direction relative to the magnetic field direction. Realizations are generated as slice planes normal to the propagation direction, which can be used directly for split-step integration of the parabolic wave equation (PWE). Although the PWE imposes no constraint on coherence along the propagation path, most statistical theories impose such constraints. Configuration-space realizations preserve scale-dependent correlation along the propagation paths, which can be used to check theoretical results.

Equivalent-phase-screens simplify theoretical computations and simulations formally by applying the path-integrated structure as a single phase perturbation initiated at a central location in the structured region. Further simplification is realized by using a two-dimensional propagation model. The two-dimensional propagation model is attractive because it characterizes one-dimensional scans that can be compared directly to diagnostic measurements.

The configuration-space model supports more realistic realizations and provides a framework for interpreting in-situ and propagation diagnostics. This paper presents new results that explore the validity of equivalent-phase-screen models for interpreting diagnostic measurements.

1 Introduction

This paper uses configuration-space realizations of ionospheric structure to simulate complex fields generated by propagation through an extended structured region using split-step integration of the parabolic wave equation (PWE) followed by free-space propagation to a measurement plane. The results are compared to free-space propagation initiated by a path-integrated structure converted to an *equivalent* phase screen. Statistical phase-screen equivalence is demonstrated in Section 3. The statistical characteristics of striation configurations are completely defined by the structure in two-dimensional slice planes. A new analytic three-dimensional structure model completely specified by two-dimensional structure is introduced in Section 4. Section 5 revisits structure diagnostics based on structure path integrals. The results can be applied directly to stochastic total electron content (TEC) measurements or theoretical calculations. Section 6 reviews the three-dimensional phase-screen theory and evaluates a tractable two-dimensional phase screen model, which has been used successfully for diagnostic measurements and strong-scatter scintillation models.

Configuration-space models are described in C. Rino, Carrano, Groves, and Yokoyama (2018). By way of review, configuration-space realizations are generated by summing contributions from field-aligned *striations*. Striations are defined in magnetic-field-aligned coordinates $[\zeta, \vec{\eta}]$ where ζ is measured along field lines and $\vec{\eta}$ is measured in a plane normal to the field line at position η. Assuming that the magnetic field lines are parallel within the data-space volume, field-aligned coordinates are generated by applying a 3×3 matrix rotation to the data-space coordinates $[x, \vec{\rho}]$. Formally,

$$\begin{bmatrix} \zeta \\ s \\ t \end{bmatrix} = \begin{bmatrix} c_{11} & c_{12} & c_{13} \\ c_{21} & c_{22} & c_{23} \\ c_{31} & c_{32} & c_{33} \end{bmatrix} \begin{bmatrix} x \\ y \\ z \end{bmatrix} . \tag{1}$$

The matrix elements c_{ij} are functions of the magnetic field direction angles in the reference coordinate system (See Appendix A).

A configuration-space realization of the electron density in the plane at $x = x_n$ is constructed as follows:

$$\Delta N(x_n, Y, Z) = \frac{1}{N_s} \sum_{k=1}^{N_s} C(k) \sigma_k^{\gamma_k} p_\perp \left(\sqrt{(S + \eta_{S_k})^2 + (T + \eta_{T_k})^2} / \sigma_k \right), \tag{2}$$

where the upper-case notation indicates an ordered coordinate collections of all the combinations of the contributing coordinate indices, sometimes referred to as a *mesh grid*. The parameters $C(k)$, σ_k, and γ_k determine the peak intensity, $C(k)\sigma_k^{\gamma_k}$, and size, σ_k, of the k^{th} striation. The profile function $p_\perp(r)$ is zero for $r > \sigma_k$ and less than one for $r < \sigma_k$. The parameters η_{S_k} and η_{T_k} determine the random locations of each striation.

The geometric dependence of realizations generated by (2) is determined by the argument of $p_\perp(r)$. From the development in C. Rino, Carrano, et al. (2018), the associated cross-field one-dimensional spectral density function (SDF) is defined by the summation

$$\Phi_{N_e}^{(1)}(q) = \frac{1}{N_s} \sum_{j=1}^{J} N^2(j) C^2(j) \sigma_j^{2\gamma_j + 1} Q_j^{(1)}(q), \tag{3}$$

where J is the number of bifurcations, $N(j)$ is the number of striation replications at each scale, $N_s = \sum_1^J N(j)$ is the total number of striations, and

$$Q_k^{(1)}(q) = \left| \int_{-\infty}^{\infty} p_\perp(y/\sigma_k) \exp\{-iyq\} dy \right|^2. \tag{4}$$

The striation parameters are selected so that (3) provides a good approximation to the two-component power-law form [1]

$$\Phi_{N_e}^{(1)}(q) \simeq C_s^{(1)} \begin{cases} q^{-\eta_1} & \text{for } q \le q_0 \\ q_0^{\eta_2 - \eta_1} q^{-\eta_2} & \text{for } q > q_0 \end{cases}. \tag{5}$$

Figure 1, which is taken from C. Rino, Carrano, et al. (2018), shows the theoretical one-dimensional SDF from (3) (red), an average of measured cross-field SDFs (blue), and the target SDF from (5). The relation between γ_n and η_n is $\gamma_n = 2\eta_n + 2$. The agreement validates the parameter selection, which is described in C. Rino, Carrano, et al. (2018).

2 Propagation Simulations

The data-space x coordinate is aligned with the propagation direction. The magnetic field direction is determined by the orientation of the striation axis in the data space volume. Integration is initiated with a plane-wave at the entry yz plane. The forward propagation equation (FPE)

$$\frac{\partial \psi(x, \vec{\rho})}{\partial x} = \Theta_k \psi(x, \vec{\rho}) + ik \Delta n(x, \vec{\rho}) \psi(x, \vec{\rho}), \tag{6}$$

characterizes the evolution of the time-harmonic scalar electromagnetic field $\psi(x, \vec{\rho})$. The phase perturbation, $k\Delta n(x, \vec{\rho})$, is generated with a frequency-dependent scaling of the electron density structure. The leading term on the right-hand side advances the field in free space:

$$\Theta\psi(x; \vec{\rho}) = \iint \widehat{\psi}(x; \vec{\kappa}) \exp\left\{ i(\kappa\rho_F)^2/2 \right\} \exp\left\{ i\vec{\rho} \cdot \vec{\kappa} \right\} \frac{d\vec{\kappa}}{(2\pi)^2}. \tag{7}$$

[1] The C_s notation here refers to electron density structure, whereby $k\Delta n$ represents a phase perturbation.

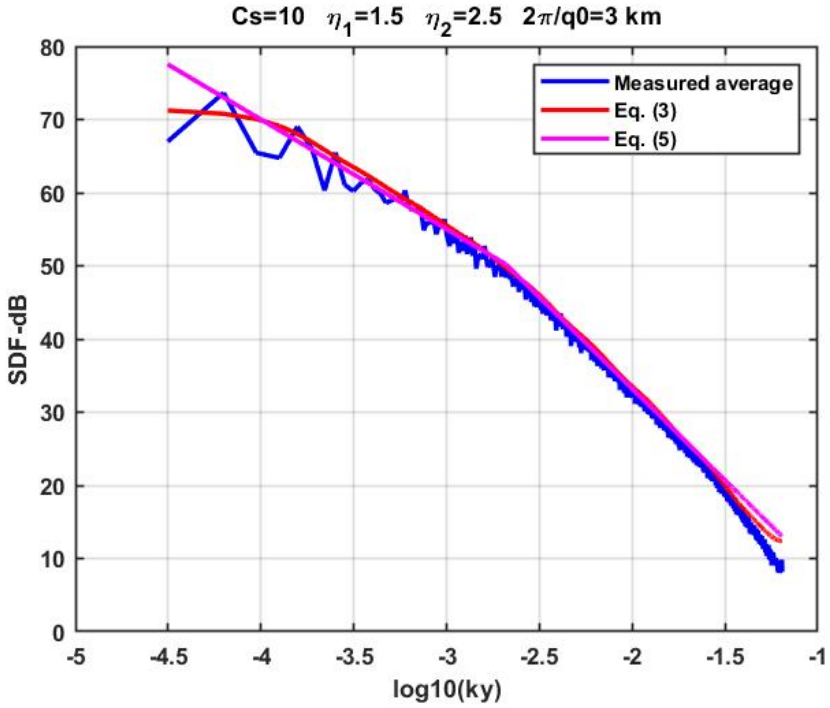

Figure 1. Measured and predicted one-dimensional cross-field SDFs.

where

$$\widehat{\psi}\,(x;\vec{\kappa}) = \iint \psi\,(x;\vec{\rho})\exp\{-i\vec{\kappa}\cdot\vec{\rho}\}d\vec{\rho} \tag{8}$$

is the two-dimensional Fourier decomposition of the slice plane field at $x = x_n$. The Fresnel scale is defined as

$$\rho_F = \sqrt{x_p/k}, \tag{9}$$

where x_p is the propagation distance from x_n, and $k = 2\pi f/c$ is the plane-wave vector magnitude at frequency f. From (7), it follows that the same free-space field would be observed at different frequencies and propagation distances that preserve ρ_F. A derivation of (6) can be found in Chapter 2 of C. L. Rino (2011).

For space-to-near-earth propagation paths it is convenient to use a fixed rectangular east-west coordinate system with the x-axis pointing downward. In that case, the PWE integration must accommodate the propagation direction relative to x. This is achieved by introducing continuous coordinate system displacement along the ray connecting the source with the plane of measurement. The SIGMA simulation developed by Deshpande, Bust, Clauer, Rino, and Carrano (2014) uses this approach. However, to the extent that the data volume boundary planes capture the structure, rotating the data space gives identical results. The two complementary coordinate systems evolved from seminal papers by Budden (1964) and Briggs and Parkin (1962).

Split-step integration converts two-dimensional slice-plane realizations into local phase perturbations, which are applied to the field at the starting point of the slice-plane increment:

$$\psi^{+}(x,\vec{\rho}) = \psi(x,\vec{\rho})\exp\{-2\pi ikK/f\Delta x\Delta N(x,\vec{\rho})\}. \tag{10}$$

The propagation operator advances $\psi^{+}(x,\vec{\rho})$ to the next slice plane, which completes the split-step integration cycle. Split-step integration and the multiple-phase-screen (MPS) method are procedurally identical. However, uncorrelated phase screens are often used

in MPS simulations. Uncorrelated phase screens are well matched to the classical theory, which presents a hierarchy of first-order differential equations that characterize the evolution of field moments in an extended medium. How local structure enters the theoretical calculations remains an important consideration. Local two-dimensional structure characterizations use the so called Markov approximation, which neglects correlation along the reference propagation direction. It is well established that MPS simulations with uncorrelated phase screens agree with classical theoretical results Knepp (1983). An alternative hybrid method developed by Gherm and Zernov (2015) avoids the Markov approximation.

3 Structure Evolution and Phase-Screen Equivalence

The striation configuration introduced in C. Rino, Carrano, et al. (2018) and summarized in Figure 1 was used for this study. The parameters are representative of equatorial night-time structure as shown in C. Rino, Yokoyama, and Carrano (2018) and references cited therein. Realizations comprised of 8176 striations were generated with magnetic field angles varying from Cross Field at 90° to Field Aligned at 0°. Striation locations were uniformly distributed within the reference plane. The yz plane dimensions are 200×50 km with 4096×4096 samples. The size of the data volume was chosen to be representative of intercepted GPS structure. Tests were run to ensure that the simulations were adequately sampled at the maximum disturbance levels. With $C_s = 10$, strong GPS L1 scintillation levels were generated in an observation plane at $x = 150$ km. The distance was chosen to capture the onset of strong scintillation. Structure is intercepted between $x = -15$ km and $x = 15$ km. The phase-screen propagation distance from the center of the region is $x = 150$ km. Four independent realizations were generated to explore the geometric dependence. Each realization used the same size distribution, but with different magnetic field orientations. Using the polar angles defined in Appendix A, the realizations will be referred to as Cross Field ($\theta_b = 90°$, $\psi_b = -90°$); Oblique In-plane ($\theta_b = 60°$, $\psi_b = -90°$); Oblique Out-of-plane ($\theta_b = 45°$, $\psi_b = -60°$); and Field Aligned ($\psi = 0°$).

For each realization split-step integration through the structured region as described Section 2 was performed followed by free-space propagation to $x = 150$ km. A second realization was constructed using the path-integrated phase applied at $x = 0$ to initiate an equivalent phase-screen simulation. The phase screen free-space propagation sampling was adjusted to coincide with the PWE free-space sampling for direct comparison. Fractional moments

$$F(m) \equiv < I(y,z)^m > / < I(y,z) >^m, \tag{11}$$

were computed for each integration and free-space propagation step. Because the FPE equations conserve intensity, verifying that $< I(y,z) >= F(1) = 1$ provides a computation integrity check. The intensity scintillation index is defined as $S4 = \sqrt{F(2) - 1}$. All the intensity samples in each two-dimensional realization were used in the fractional moment computations.

Figures 2, 3, 4, and 5 summarize the intensity structure evolution. The solid red lines in the left frames show the $S4$ estimates from split-step integration. The open red circles show the $S4$ estimates from the subsequent free-space propagation. The phase-screen calculation is implemented by bypassing the propagation step, whereby each field increment is a phase perturbation. At the exit plane the field is propagated from $x = 0$ to 150 km. The middle and right frames show intensity and phase realizations derived from the $z = 0$ scan of the complex field in the observation plane at $x = 150$ km, which includes 135 or 150 km free-space propagation, respectively. Continuous phase records are constructed by removing 2π phase jumps.

The free-space $S4$ intensity evolution is nearly identical for the PWE field and the phase-screen field. Moreover, the intensity and phase structure from central scans in the

observation planes are empirically similar. Evidently, the dominant statistical variation is determined by the overall structure distribution rather than where structures are intercepted within the disturbed region. SDFs will be compared in Section 6.

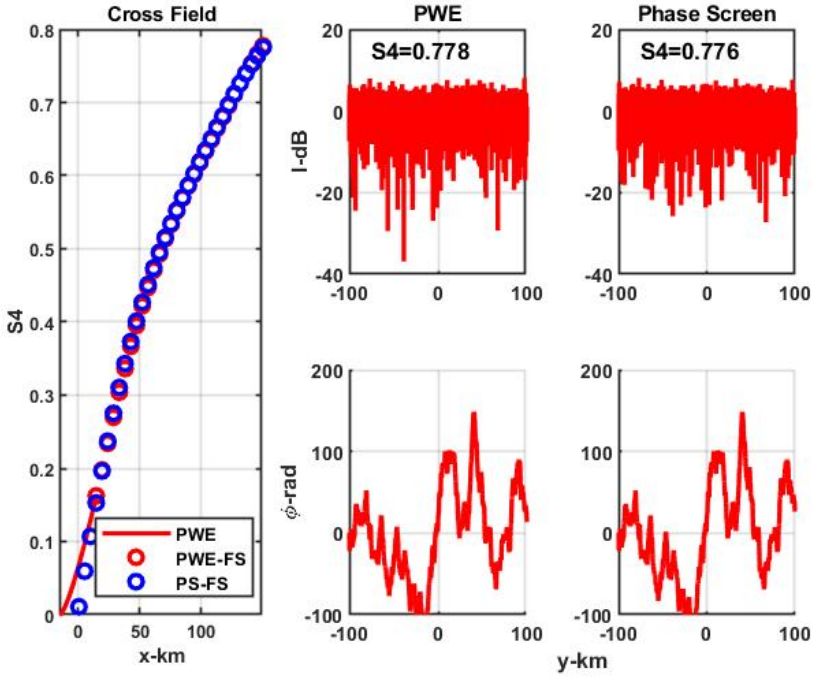

Figure 2. Cross Field summary. Left frame shows $S4$ for split-step (red) and phase-screen (blue). Middle and right frames show split-step and phase screen intensity and phase from central observation-plane scan.

The Field Aligned realization shows much more complicated intensity and phase patterns. The Field Aligned path-integrated structure is a scaled version of any one of the identical slice contributions. Although it is well known that coherent path integration enhances scintillation, the fact that the enhancement is realized with an equivalent phase screen was not expected. The structure of the Field-Aligned realization appears to be driven by large cumulative phase gradients rather than cumulative diffraction effects.

To explore this further, the upper frame of Figure 6 shows the Field Aligned intensity in the observation plane. The intensity pattern shows a fairly uniform background with a complex pattern of local intensity reductions. The fractional moments beyond $m = 2$ are much larger than $F(m) = m!$, which corresponds to an exponential distribution. This implies large departures from Gaussian intensity statistics. The lower frame shows a zoomed square region. The individual striations are cylindrical but overlapping, whereby intricate diffraction patterns are created. However, because of the ionosphere refractive index decreases with increasing density, local lens-like action tends to deflect rays away from the most dense regions, which explains intuitively how the deep field intensity reductions are created. The phase structure appears to contain uncorrected phase jumps. Even so, the sampling is adequate to support the PWE calculation of the complex field. Whether these results could be reproduced with real measurements is problematic because strict invariance along field lines is an idealization. The model can accommodate

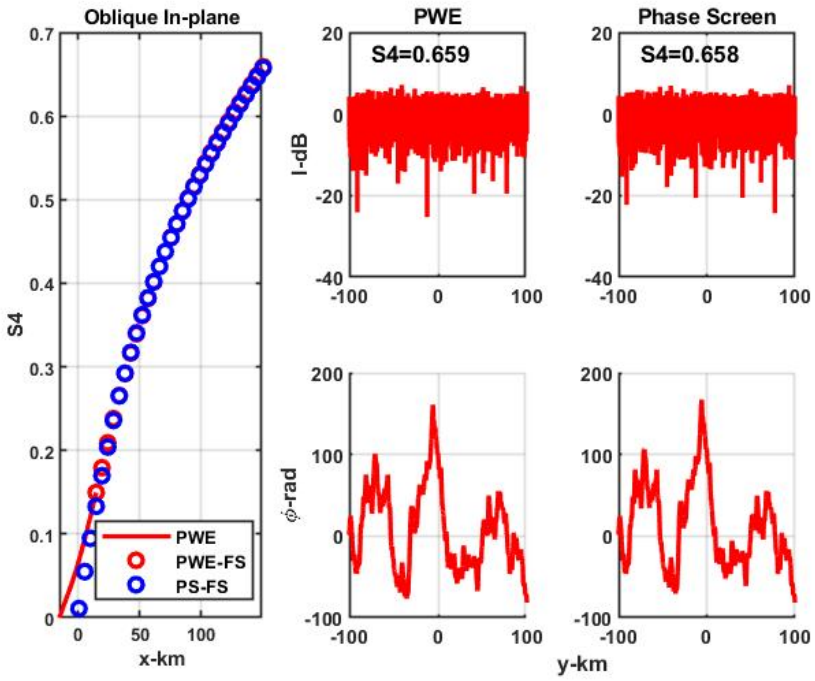

Figure 3. Oblique In-plane summary. Left frame shows $S4$ for split-step (red) and phase-screen (blue). Middle and right frames show split-step and phase screen intensity and phase from central observation-plane scan.

field-line curvature and field-aligned density variation as improved structure models provide guidelines.

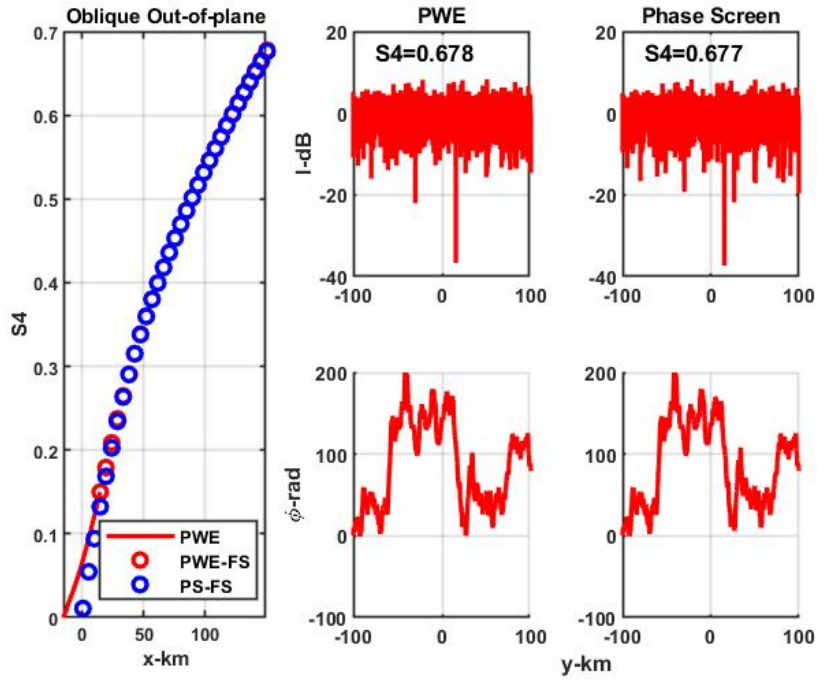

Figure 4. Oblique Out-of-plane summary. Left frame shows $S4$ for split-step (red) and phase-screen (blue). Middle and right frames show split-step and phase screen intensity and phase from central observation-plane scan.

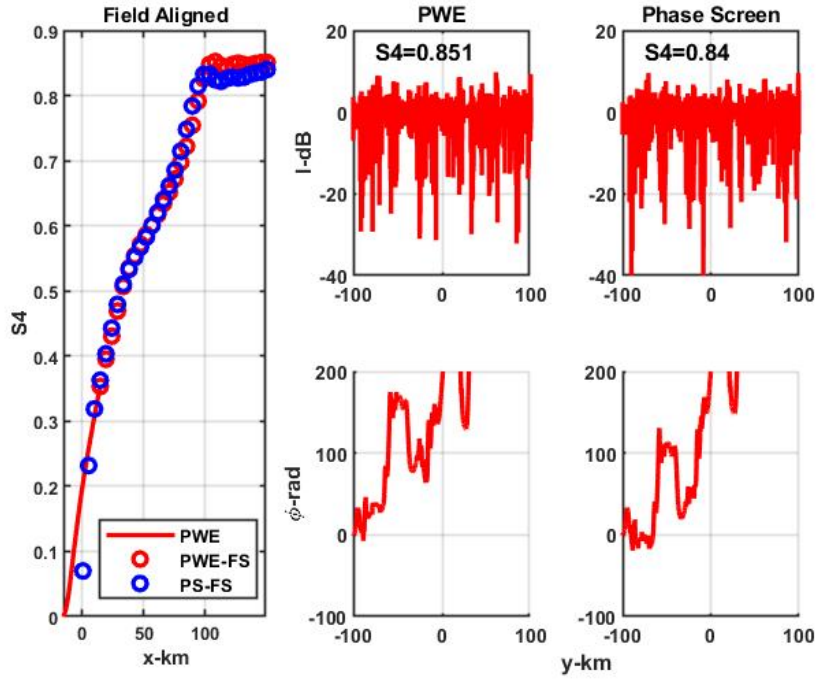

Figure 5. Field Aligned summary. Left frame shows $S4$ for split-step (red) and phase-screen (blue). Middle and right frames show split-step and phase screen intensity and phase from central observation-plane scan.

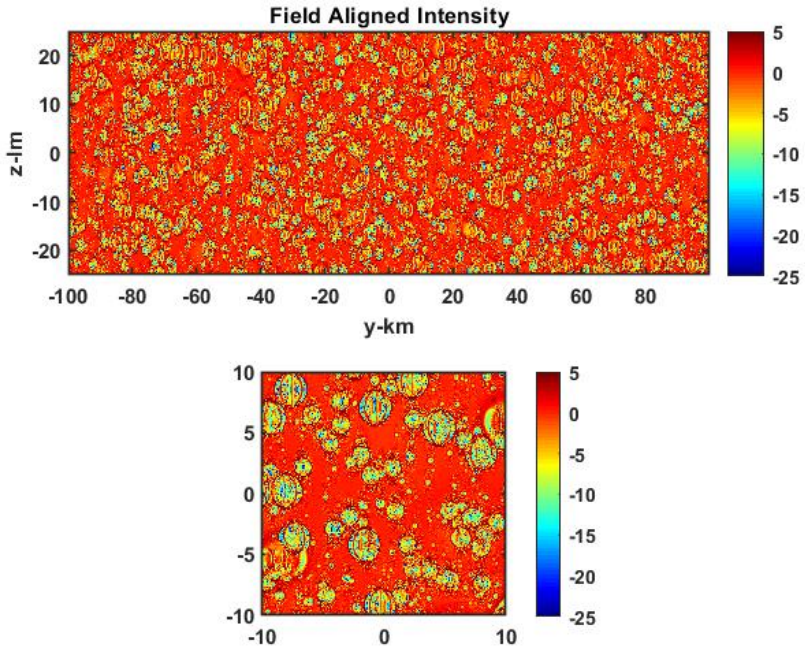

Figure 6. Upper frame shows Field Aligned intensity in observation plane. Lower frame is zoomed view with square axes

4 A New Ionospheric Structure Model

Ionospheric structure models provide a parameterized analytic characterization of the three-dimensional ionospheric electron density structure. The most commonly used statistical measure is an SDF, which is formally the expectation of a spatial Fourier decomposition of the structure. Configuration-space realizations defined by (3) are fully three dimensional. The uniform spatial distribution of the striations guarantees well-defined averages of statistical measures. The one-dimensional SDF, which is reproduced here as (3), is used as a defining relation to make direct comparisons to one-dimensional in situ diagnostic measurements.

With the configuration parameters specified, two-dimensional and three-dimensional SDFs can be calculated as follows:

$$\Phi_{N_e}(\kappa_x, \vec{\kappa}) = \frac{1}{N_s} \sum_{j=1}^{J} N^2(j) C^2(j) \sigma_j^{2\gamma_j + (3-n)/2} Q_j(\kappa_x, \vec{\kappa}), \tag{12}$$

where the dimension $n = 1$, 2, or 3. The integrations in

$$Q_k(\kappa_x, \vec{\kappa}) = \left| \int \cdots \int \; p_\perp(\sqrt{(s^2 + t^2)}/\sigma_k) \exp\{-i(x\kappa_x + \vec{\rho} \cdot \vec{\kappa})\} dx d\vec{\rho} \right|^2 . \tag{13}$$

are defined consistently. The cross-field variables, s and t, are functions of x, y, and z as defined by the second and third rows in (1). The factor $\sigma_j^{2\gamma_j + (3-n)/2)}$ establishes SDF dimensions such that integration over all spatial wavenumbers reproduces electron-density variance. The defining one-dimensional SDF of a y scan can be computed alternatively by integrating the three-dimensional SDF over the unscanned wavenumbers:

$$\Phi_{N_e}^{(1)}(\kappa_y) = \iint \Phi_{N_e}(\kappa_x, \kappa_y, \kappa_z) \frac{d\kappa_z}{2\pi} \frac{d\kappa_x}{2\pi}. \tag{14}$$

Although a configuration-space realization is fully three dimensional as is the Fourier transform in (13), the stochastic structure is defined by the two-dimensional cross-field SDF. For cross-field realizations, which have no variation along z, and field-aligned realizations, which have no variation along x, the following formal results show the defining relation in terms of two-dimensional SDFs directly:

$$\Phi_{N_e}(\kappa_x, \vec{\kappa}) = \begin{cases} \Phi_{N_e}(\kappa_x, \kappa_y) 2\pi\delta(\kappa_z) \\ \Phi_{N_e}(\kappa_y, \kappa_z) 2\pi\delta(\kappa_x) \end{cases} \tag{15}$$

Because of the cylindrical symmetry of the profile functions and their uniform distribution, the two-dimensional isotropic cross-field SDFs are identical.

The upper frame of Figure 7 shows $\Phi_{N_e}(\kappa_x, \kappa_y, 0)$ as computed from (12) for the cross-field geometry. For the non-zero κ_z values, $\Phi_{N_e}(\kappa_x, \kappa_y, \kappa_z) = 0$, which is in agreement with the upper form of (15). The lower frame shows calculations of the one-dimensional SDF from (3) (blue) and from a numerical integration of the three-dimensional SDF (red) defined by (12). The following two-dimensional analytic form reproduces two-dimensional and one-dimensional relations:

$$\Phi_{N_e}(\vec{\kappa}) \simeq C_s^{(2)} \begin{cases} \kappa^{-p_1} & \text{for } \kappa \le \kappa_0 \\ \kappa_0^{p_2 - p_1} \kappa^{-p_2} & \text{for } \kappa > \kappa_0 \end{cases}, \tag{16}$$

where $p_n = \eta_n + 1$.

Upon applying the coordinate transformation summarized in Appendix A, (16) becomes an alternative to the model introduced in Chapter 3.1.4 of C. L. Rino (2011) for the three-dimensional electron density SDF. The earlier model starts with a three-dimensional isotropic form with transformations that generate ellipsoidal contours of constant correlation or products of along-field and cross-field SDF components. The configuration-space model is *defined* in the spectral domain over a finite range of contributing scales.

Consequently, only the defining SDF parameters and the magnetic field direction need be specified. The largest and smallest contributing scales determine the contributing scale range. The current model has no field-aligned variation within the data space.

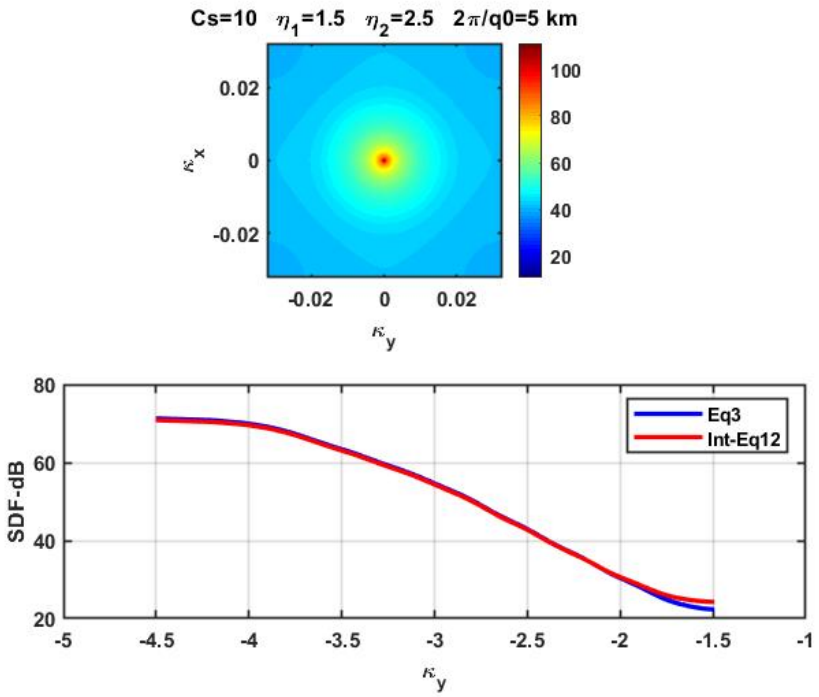

Figure 7. The upper frame shows the two-dimensional spectral density function computed from (12) for the Cross Field geometry. The lower frame shows the agreement of two calculations of the one-dimensional spectral density function.

5 Propagation Models

Propagation diagnostics are effectively one-dimensional time series generated by the combined effects of the motion of the propagation path and the motion of the structure. It is generally assumed that intermediate-scale structure from tens of kilometers to hundreds of meters is frozen over measurement intervals, whereby time-to-space conversion defines a linear scan of a diffraction pattern. The structure drift and the propagation distance to the structured region are generally not known. However, data-space realizations over a range of structure orientations provide a framework for exploring propagation diagnostics.

Complex-field measurements provide the signal intensity and phase diagnostics. Navigation satellite phase measurements are routinely converted to TEC. The following model is used to convert continuous phase to TEC:

$$\Delta\phi(\vec{\rho}) = -2\pi K/f \int_0^L \Delta N_e(x, \vec{\rho})dx, \tag{17}$$

where $K = 1.3454{\times}10^9 m^2/s$ and L is a measure of the structure extent. Invoking phase-screen equivalence, the complex field

$$\psi = \exp\{i\Delta\phi(\vec{\rho})\} \tag{18}$$

captures the interaction of the field with the structured ionosphere. Intensity structure develops as the field propagates in free space, whereby scaled TEC is the initiating structure from which intensity scintillation evolves.

In Appendix B is shown that the two-dimensional SDF of the path-integrated phase can be computed as follows:

$$\Phi_{\Delta\phi}(\vec{\kappa}) = (2\pi KL/f)^2 \int_{-\infty}^{\infty} \frac{\sin^2(\kappa_x L/2)}{(\kappa_x L/2)^2} \Phi_{N_e}(\kappa_x, \vec{\kappa}) \frac{d\kappa_x}{2\pi}. \tag{19}$$

If the κ_z variation is uniform over the spatial wavenumber range to $2\pi/L$, which implies decorrelation of the structure along the propagation path,

$$\Phi_{\Delta\phi}(\vec{\kappa}) \simeq (2\pi KL/f)^2 \Phi_{N_e}(0, \vec{\kappa}). \tag{20}$$

This is the usual assumption for interpreting scintillation measurements. However, numerical integration of (19) shows that the path-integrated structure can be more complicated.

Figure 8 summarizes the path-integrated structure for the Cross Field, Oblique Out-of-plane, and Field Aligned configurations. The Cross Field structure has no variation along the z axis, which lies along the magnetic field direction. The oblique geometry has significant yz variation. The Field Aligned geometry reproduces a scaled version of the unchanging two-dimensional structure. Figure 9 shows the corresponding SDFs derived from (16) with transformations that accommodate the field orientation. The cross-field SDF is one-dimensional and confined to $K_z = 0$. The Oblique Out-of-plane SDF has tilted elliptical contours of constant spectral intensity. The Field Aligned SDF is isotropic, and identical to the upper frame of Figure 7, which was derived directly from (12).

To the extent that TEC can be measured directly and allowing for time-to-space conversion, one-dimensional TEC SDFs can be constructed. Figure 10 shows the one-dimensional SDFs derived by numerically integrating (19). The cross-field variation reproduces the canonical phase SDF, namely the κ_y variation of (16), whereby there is a direct relation between measured and structure model parameters. For oblique geometries the varying correlation along the propagation path significantly changes the relation between the in situ SDF and the measured one-dimensional SDFs. The ramifications for propagation diagnostics is discussed in the next section.

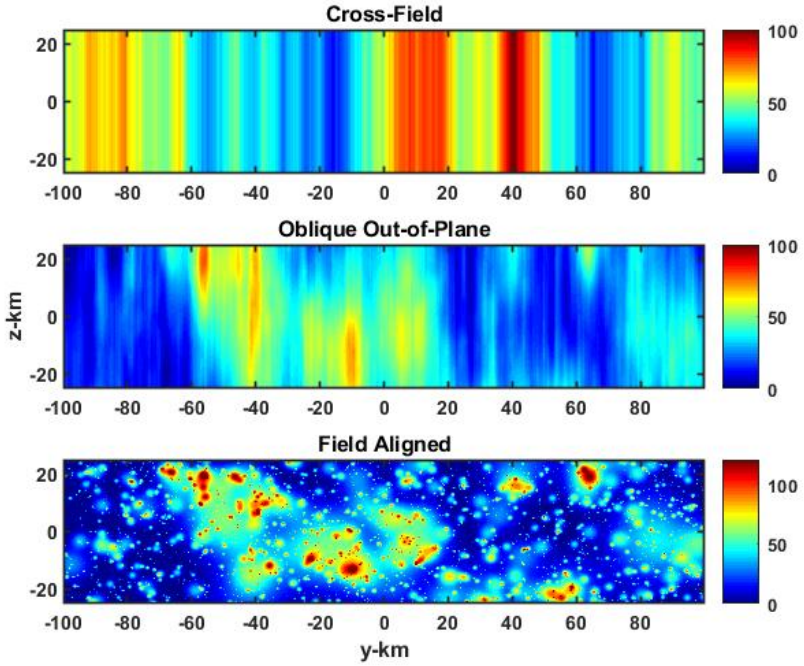

Figure 8. Path-integrated intensity realization examples.

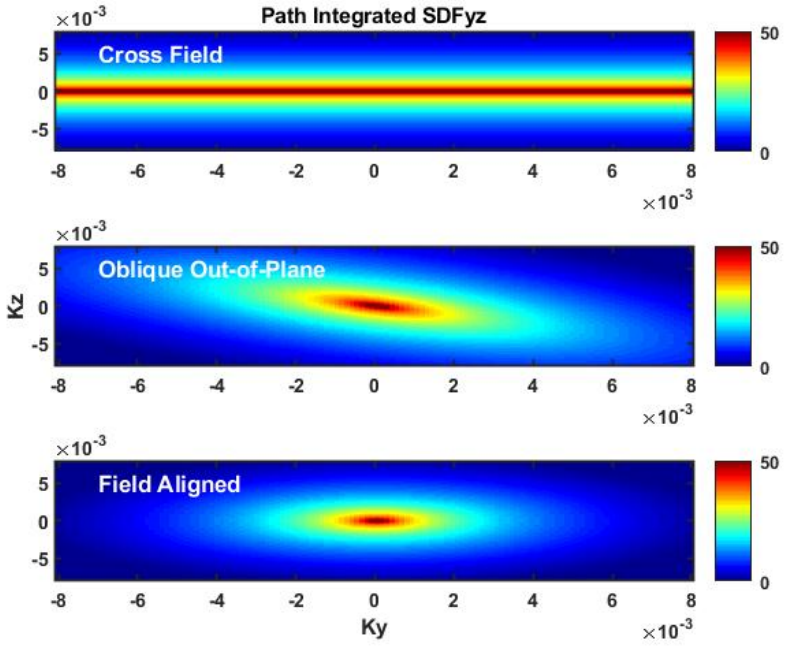

Figure 9. Path-integrated two-dimensional spectral density function (SDF) from 19.

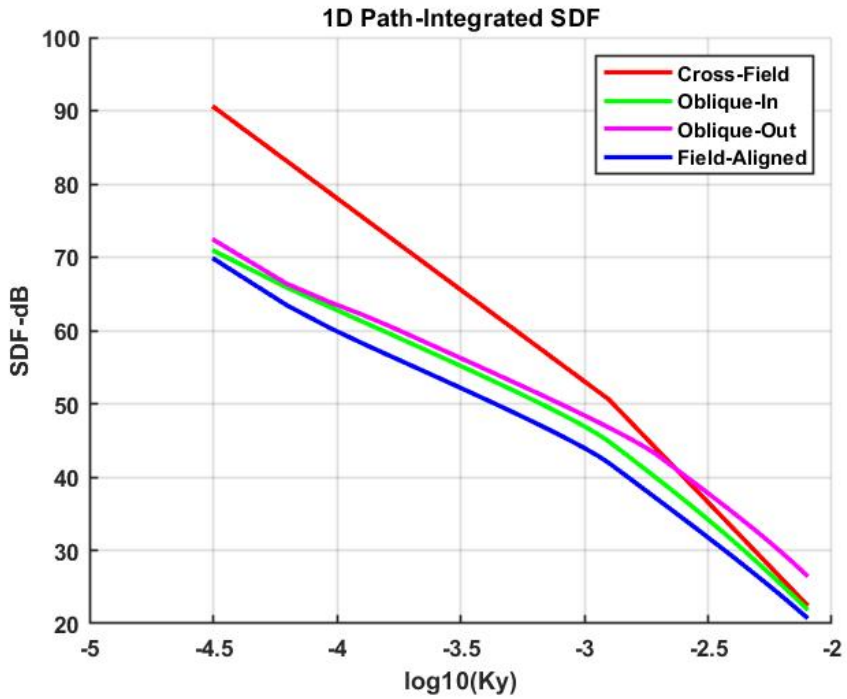

Figure 10. One-dimensional y spectral density function (SDF)

6 Propagation Diagnostics

Phase-screen equivalence greatly simplifies the interpretation of propagation diagnostics. Irrespective of the phase statistics, as long as the structure has sufficient homogeneity to supports an SDF characterization, $\Phi_{\Delta\phi}(\vec{\kappa})$, the intensity SDF in the measurement plane can be computed as follows:

$$\Phi_I(\vec{\kappa}) = \iint \left[\exp\left\{-Lk^2 g\left(\vec{\alpha}, \vec{\kappa}\rho_F^2\right)\right\} - 1\right] \exp\left\{-i\vec{\kappa}\cdot\vec{\alpha}\right\} d\vec{\alpha}. \tag{21}$$

where

$$g(\vec{\alpha}_1, \vec{\alpha}_2) = 8k^2 \iint \Phi_{\Delta\phi}(\vec{\kappa}) \sin^2\left(\kappa\cdot\vec{\alpha}_1/2\right) \sin^2\left(\kappa\cdot\vec{\alpha}_2/2\right) d\kappa/(2\pi)^2, \tag{22}$$

and

$$SI^2 = \iint \Phi_I(\vec{\kappa}) d\vec{\kappa}/\left(2\pi\right)^2. \tag{23}$$

A derivation can be found in Chapter 3.4 of C. L. Rino (2011). Although the problem is well posed, a nested double integration is required to calculate $\Phi_I(\vec{\kappa})$ with another integration to calculate the one-dimensional SDF. At the present time there is no tractable means of using these results directly for interpreting intensity scintillation diagnostics. Under weak-scatter conditions the result converges to the well known weak-scatter result that has been used, together with(20), for interpreting most diagnostic measurements.

A tractable two-dimensional propagation theory was developed by Carrano and Rino (2016). The two-dimensional theory is formally obtained from (21) when

$$\Phi_{\Delta\phi}(\vec{\kappa}) = 2\pi\delta(\kappa_z)\Phi_{\Delta\phi}(\kappa_y), \tag{24}$$

which applies to the Cross Field realization shown in the upper frame of Figure 19. For oblique geometries it is tacitly assumed that the structure can be characterized by an equivalent phase-screens as well. Irregularity parameter estimation (IPE) procedures varies phase-screen parameters to provide a best fit to a measured intensity SDF C. Rino and Carrano (2018). The existence of an equivalent phase screen can be demonstrated by back propagating the complex field to minimize the intensity scintillation. Back propagation was demonstrated by Carrano, Groves, Delay, and Doherty (2014). The two-dimensional form of (7) is

$$\Theta\psi(x;y) = \int \widehat{\psi}(x;\kappa) \exp\left\{i\kappa^2 x_p/(2k)\right\} \exp\left\{iy\kappa\right\} \frac{d\kappa}{2\pi}. \tag{25}$$

Back propagation applies (25) with increasing negative x_p values until the intensity fluctuation is minimized.

Back propagation was applied to the one-dimensional complex fields extracted from all four realizations. No significant intensity structure reduction was obtained for the isotropic Field Aligned realization. Figure 11 shows the reconstructed phase from the back-propagated complex fields (red), which are overlaid on the path-integrated phase (blue). The minimum $S4$ is shown on each plot. The minimum value of $S4$, ideally zero, is a quantitative measure of phase-screen equivalence. The back-propagated phase differences are smallest for the oblique geometries, whereas the largest S4 reduction is achieved with the Cross Field realization. The back-propagation distances to intensity minima, are 147.84 km Cross Field, 157.99 km Oblique In-plane, and 157.35 km Oblique Out-of-plane, are close to the nominal phase-screen distance of 150 km.

The back-propagated results show that as long as the propagation direction is not close to field alignment, an equivalent phase screen can be constructed with back-propagated phase close to the path-integrated phase. Regarding parameter estimation, the upper frame of Figure 12 shows the z average of measured one-dimensional intensity SDFs in the measurement plane. The expectation SDF should not change with z. However, the differing fluctuation levels reflect the varying z correlation. Because of the intrinsic low-pass filtering of the intensity structure, periodogram estimation can be applied directly.

The lower frame shows the correspond phase SDFs. Prior to periodogram computation, the linear component connecting the phase end points was subtracted. The blue overlay is derived from a segmented log-log linear fit. The spectral index estimates, $p_1 = 2.2$ and $p_2 = 3.0$, are reasonably close to the expected values $p_1 = 2.5$ and $p_2 = 3.5$.

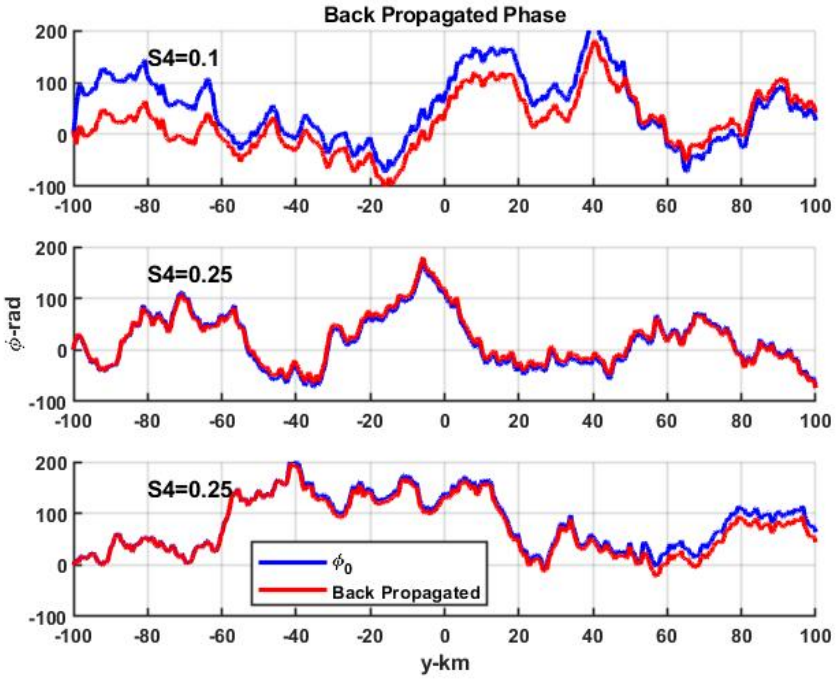

Figure 11. Back propagated phase (red) with path-integrated phase scan overlaid (blue). Text is minimum $S4$. Upper frame is Cross Field, middle frame is Oblique In-Plane, lower frame is Oblique Out-of-Plane.

The results suggest that the SDF of the back-propagated phase reproduces the result that would be expected if contributions to the path integration are uncorrelated. However, to the extent that the phase-screen SDF is determined by (19), we would expect the back-propagated phase to vary as shown in Figure 10). It appears that propagation effects within the layer, which were are not considered in (19), are influencing the result. The argument is that uncorrelated results only apply to the large-scale, which maps directly onto the phase. For that scale range,

$$\Phi_{\Delta\phi}(\vec{\kappa}) \simeq (2\pi KL/f)^2 \int_{-\infty}^{\infty} \Phi_{N_e}(\kappa_x, \vec{\kappa}) \frac{d\kappa_x}{2\pi}, \tag{26}$$

applies. For smaller-scale structure affected by diffraction (20) applies. A similar argument has been applied to justify the use of the Markov approximation to derive field moment equations. Under phase-screen equivalence, correlated large-scale structure is unaffected by diffraction. Only uncorrelated small-scale structure is influencing cumulative development of intensity scintillation and the phase structure that supports it.

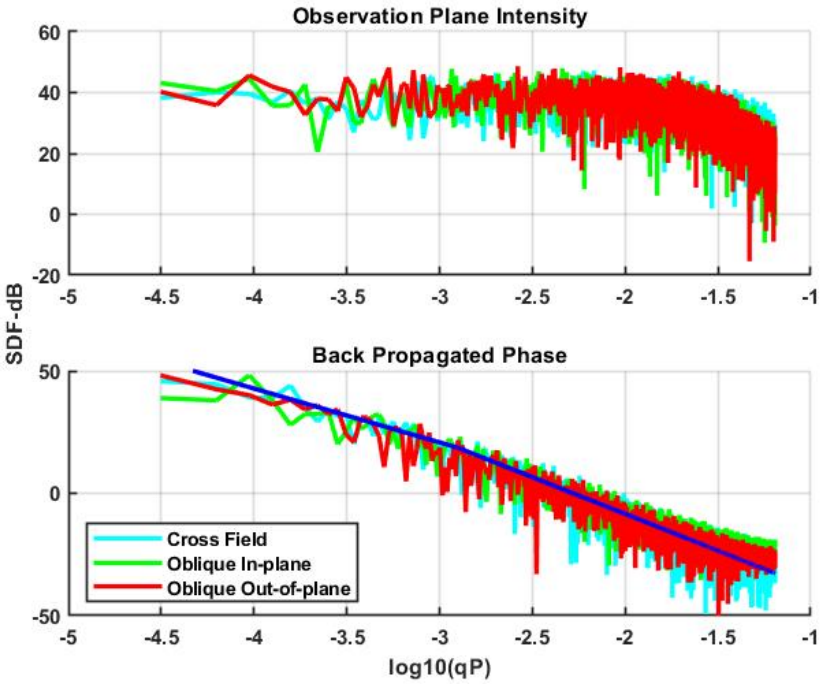

Figure 12. Each frame shows the back-propagated phase (red) overlaid on the phase derived from the PWE integration (red)

7 Summary and Discussion

This paper used configuration-space realizations to explore the geometric dependence of propagation through extended ionospheric structure. The study was undertaken to investigate the validity of the equivalent-phase-screen model, which was introduced in the seminal paper H. G. Booker, Ratcliffe, and Shinn (1950). A later paper made theoretical comparisons between extended-media and phase-screen theories H. Booker, Ferguson, and Vats (1985). Variants of the phase-screen model are invariably used in scintillation models such as WBMOD Secan, Bussey, Fremouw, and Basu (1995), PBMOD Retterer (2010), and Wernik, Alfonsi, and Materassi (2007). Our results show the phase screen model is surprisingly robust. In can be used to extend models to accommodate strong scatter although extreme scattering conditions have yet to be investigated.

In Section 4 a new three-dimensional electron density SDF model was introduced for field-aligned structure. Models based on analytic forms that admit closed-form integration, such as Shkarofsky (1968), necessarily introduce a number of parameters that have no impact on the structure defined by the largest and smallest striation scales. The electron density SDF model was developed to facilitate theoretical calculations of measurable quantities, most directly TEC. In Section 5 is was shown that one-dimensional stochastic TEC SDFs are sensitive to the orientation of the path integration relative to the magnetic field. It might be expected that this dependency would carry over to the intensity scintillation SDF. However, fully three-dimensional calculations to explore this dependency remain intractable.

Section 6 explored propagation diagnostics derived from one-dimensional measurements of the complex field. There is no theory that addresses phase directly, but the phase-screen theory provides an analytic connection between an *equivalent* phase screen and measurable intensity structure. By using back propagation we were able to show that there is a *equivalent* one-dimensional phase screen as long as the propagation direction is not approaching field alignment. Furthermore, we found the shape of the equivalent phase-screen SDF is insensitive to oblique geometry, whereby the standard phase-screen scintillation can be used. The results are encouraging in that they supports IPE applications Carrano, Rino, and Groves (2017) and GPS phase-screen models C. Rino, Breisthc, et al. (2018).

A Rotation Matrix

Let $\vec{u}_b$ represent a unit vector along the magnetic field direction in the data space coordinate system. In terms of polar angles

$$\vec{u}_b = [\cos(\theta_b), \sin(\theta_b)\cos(\phi_b), \sin(\theta_b)\sin(\phi_b)]. \tag{A.1}$$

The 3×3 matrix$C$ that transform $C\vec{u}_b$ to a unit vector rotates a vector in the data space to a field-aligned coordinate system with principal axes aligned with $\vec{u}_b$. The elements are

$$\begin{aligned}
c_{11} &= \cos(\theta) && \text{(A.2)}\\
c_{12} &= \sin(\theta)\cos(\psi) && \text{(A.3)}\\
c_{13} &= \sin(\theta)\sin(\psi) && \text{(A.4)}\\
c_{21} &= -\sin(\theta) && \text{(A.5)}\\
c_{22} &= \cos(\theta)\cos(\psi) && \text{(A.6)}\\
c_{23} &= \cos(\theta)\sin(\psi) && \text{(A.7)}\\
c_{31} &= -\sin(\psi) && \text{(A.8)}\\
c_{32} &= \cos(\psi) && \text{(A.9)}\\
c_{23} &= 0 && \text{(A.10)}\\
& && \text{(A.11)}
\end{aligned}$$

B Derivation of (19)

Let

$$\Delta N_e(x,\vec{\rho}) = \int_{-\infty}^{\infty}\iint \widehat{\Delta N}(\kappa_x,\vec{\kappa})\exp\{-i\kappa_x x\}\exp\{-i\vec{\kappa}\cdot\vec{\rho}\}\frac{d\vec{\kappa}}{(2\pi)^2}\frac{d\kappa_x}{2\pi}. \tag{B.1}$$

Using the formal property

$$\iint \exp\{-i\left(\vec{\kappa}-\vec{\kappa}'\right)\cdot\vec{\rho}\}d\vec{\rho} = (2\pi)^2\,\delta\left(\vec{\kappa}-\vec{\kappa}'\right), \tag{B.2}$$

it follows that

$$\widehat{\Delta\phi}(\vec{\kappa}) = -2\pi K/f_c\int_{-\infty}^{\infty}\widehat{\Delta N}(\kappa_x,\vec{\kappa})\int_0^L \exp\{-i\kappa_x x\}dx\frac{d\kappa_x}{2\pi} \tag{B.3}$$

The integral over x can be evaluated analytically:

$$\int_0^L \exp\{-i\kappa_x' x\}dx = \exp\{-i\kappa_x L/2\}L\sin(\kappa_x L/2)/\left(\kappa_x L/2\right), \tag{B.4}$$

which reduces the two-dimensional Fourier transform to

$$\widehat{\Delta\phi}(\vec{\kappa}) = -\left(2\pi K/f_c\right)L\int_{-\infty}^{\infty}\exp\{-i\kappa_x L/2\}\sin(\kappa_x L/2)/\left(\kappa_x L/2\right)\widehat{\Delta N}(\kappa_x,\vec{\kappa})\frac{d\kappa_x}{2\pi}. \tag{B.5}$$

Using the uncorrelated increments property of $\widehat{\Delta N}(\kappa_x,\vec{\kappa})$,

$$\left\langle\left|\widehat{\Delta\phi}(\vec{\kappa})\right|^2\right\rangle = \left(2\pi K/f_c\right)^2 L^2\int_{-\infty}^{\infty}\sin^2(\kappa_x L/2)/\left(\kappa_x L/2\right)^2\Phi(\kappa_x,\vec{\kappa})\frac{d\kappa_x}{2\pi}. \tag{B.6}$$

Acknowledgments

Enter acknowledgments, including your data availability statement, here.

References

Booker, H., Ferguson, J., & Vats, H. O. (1985). Comparison between the extended-medium and the phase-screen scintillation theories. *J. of Atmospheric and Terrestial Physics*, *47*(4), 391-399.

Booker, H. G., Ratcliffe, J. A., & Shinn, D. H. (1950). Diffraction from an irregular screen with applications to ionospheric problems. *Proc. Camb. Phil. Soc.*, *242 A*, 579-607.

Briggs, B. H., & Parkin, I. A. (1962). On the variation of radio star and satellite scintillations with zenith angle. *J. Atmos. and Terr. Phys.*, *25*, 339-365.

Budden, K. G. (1964). The amplitude fluctuations of the radio wave scattered from a thick ionospheric layer with weak irregularities. *J. Atmos. and Terr. Phys.*, *27*, 155-172.

Carrano, C. S., Groves, K. M., Delay, S. H., & Doherty, P. H. (2014). An inverse diffraction technique for scaling measurements of ionospheric scintillations on the gps L1, L2, and L5 carriers to other frequencies. In *Proceedings of the 2014 institute of navigation ion itm meeting san diego, calif.* Institute of Navigation.

Carrano, C. S., & Rino, C. L. (2016). A theory of scintillation for two-component power law irregularity spectra: Overview and numerical results. *Radio Sci.*, *51*(doi:10.1002/2015RS005903), 789813.

Carrano, C. S., Rino, C. L., & Groves. (2017). Maximum likelihood estimation of phase screen parameters from ionospheric scintillation spectra. *15th International Ionospheric Effects Symposium, PAGES=1-11, Alexandria, VA, May 9-11*.

Deshpande, K. B., Bust, G. S., Clauer, C. R., Rino, C. L., & Carrano, C. S. (2014). Satellite-beacon ionospheric-scintillation globalmodel of the upper atmosphere (sigma) i: High-latitude sensitivity study of the model parameters. *J. Geophys. Res. Space Physics*, *119*(doi:10.1002/2013JA019699), 40264043.

Gherm, V. E., & Zernov, N. N. (2015). Strong scintillation of gnss signals in inhomogeneous ionosphere: 2. computer simulator of random signals. *Radio Science*, *50*(doi:10.1002/2014RS005604), 168176.

Knepp, D. L. (1983). Multiple phase-screen calculation of the temporal behavior of stochastic waves. *Radio Sci.*, *71*(6).

Retterer, J. M. (2010). Forecasting low latitude radio scintillation with 3-d ionospheric plume models: 2. scintillation calculation. , *115*(doi:10.1029/2008JA013840).

Rino, C., Breisthc, B., Morton, Y., Jiao, Y., Xu, D., & Carrano, C. (2018). A compact multifrequency gnss scintillation model. *Institute of Navigation Journal*, 1-7. (DOI: 10.1002/navi.263)

Rino, C., & Carrano, C. (2018). On the characterization of intermediate-scale ionospheric structure. *Radio Science*. (10.1029/2018RS006709)

Rino, C., Carrano, C., Groves, K., & Yokoyama, T. (2018). A configuration-space model for intermediate-scale ionospheric structure. *Radio Science*. (Accepted for Publication)

Rino, C., Yokoyama, T., & Carrano, C. (2018). Dynamic spectral characteristics of high-resolution simulated equatorial plasma bubbles. *Progress in Earth and Planetary Science*. (Submitted for publication)

Rino, C. L. (2011). *The theory of scinillation with applications in remote sensing.* Wiley.

Secan, J. A., Bussey, R. M., Fremouw, E. J., & Basu, S. (1995). An improved model of equatorial scintillation. *Radio Science*, *30*(3), 607-617.

Shkarofsky, I. P. (1968). Generalized Turbulence Space-Correlation and Wave-Number Spectrum-Function Pairs. *Can. J. Phys.*, *46*, 2683-2153.

Wernik, A. W., Alfonsi, L., & Materassi, M. (2007). Scintillation modeling using in situ data. *Radio Sci.*. (doi:10.1029/2006RS003512)